Supplementary Materials

A flexible multimodal sensor with intrinsic signal decoupling for wearable respiratory monitoring

Ziyang Song[1,2,3], Chen Huang[1], Evgeniya Sheremet[4], Raul D. Rodriguez[4], Liangjing Shi[2], Yin Cheng[2], Jing Sun[2], Guan-E Wang[5,*], Ranran Wang[1,2,*]

[1]School of Chemistry and Materials Science, Hangzhou Institute for Advanced Study, University of Chinese Academy of Sciences, Hangzhou 310024, Zhejiang, China.
[2]State Key Laboratory of High Performance Ceramics, Shanghai Institute of Ceramics, Chinese Academy of Sciences, Shanghai 200050, China.
[3]Center of Materials Science and Optoelectronics Engineering, University of Chinese Academy of Sciences, Beijing 100049, China.
[4]Tomsk Polytechnic University, Tomsk 634050, Russia.
[5]State Key Laboratory of Structural Chemistry, Fujian Institute of Research on the Structure of Matter, Chinese Academy of Sciences, Fuzhou 350002, Fujian, China.

[*]**Correspondence to:** Prof. Guan-E Wang, State Key Laboratory of Structural Chemistry, Fujian Institute of Research on the Structure of Matter, Chinese Academy of Sciences, Fuzhou 350002, Fujian, China. E-mail: gewang@fjirsm.ac.cn; Prof. Ranran Wang, State Key Laboratory of High Performance Ceramics, Shanghai Institute of Ceramics, Chinese Academy of Sciences, Shanghai 200050, China. E-mail: wangranran@mail.sic.ac.cn

Supplementary Figures

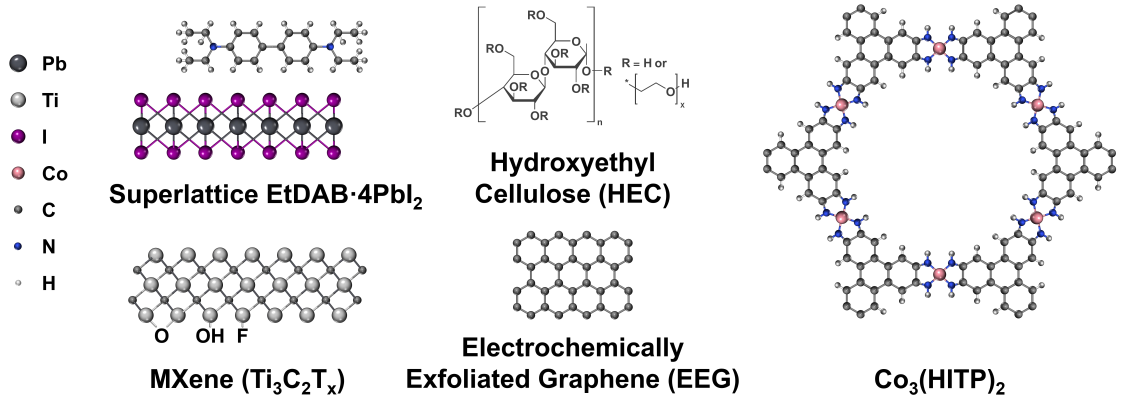

Supplementary Figure 1. Chemical structures and compositions of the functional materials used in each sensing module, including MXene ($Ti_3C_2T_x$), EtDAB·$4PbI_2$, electrochemically exfoliated graphene (EEG), hydroxyethyl cellulose (HEC) and $Co_3(HITP)_2$.

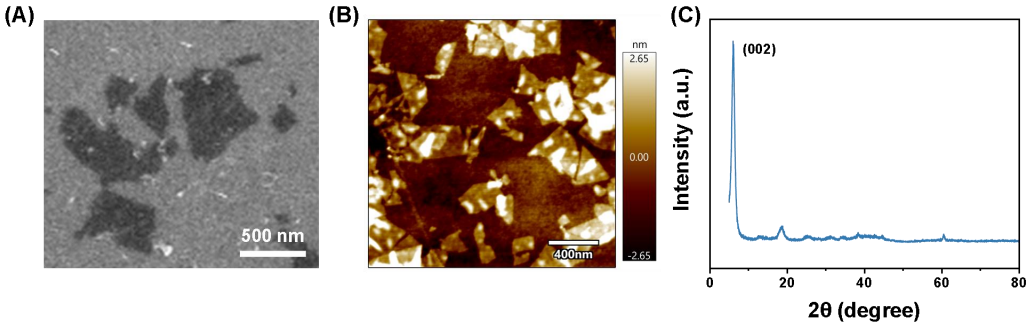

Supplementary Figure 2. (A) SEM image and (B) AFM image of MXene ($Ti_3C_2T_x$) sheets. (C) XRD spectra of MXene.

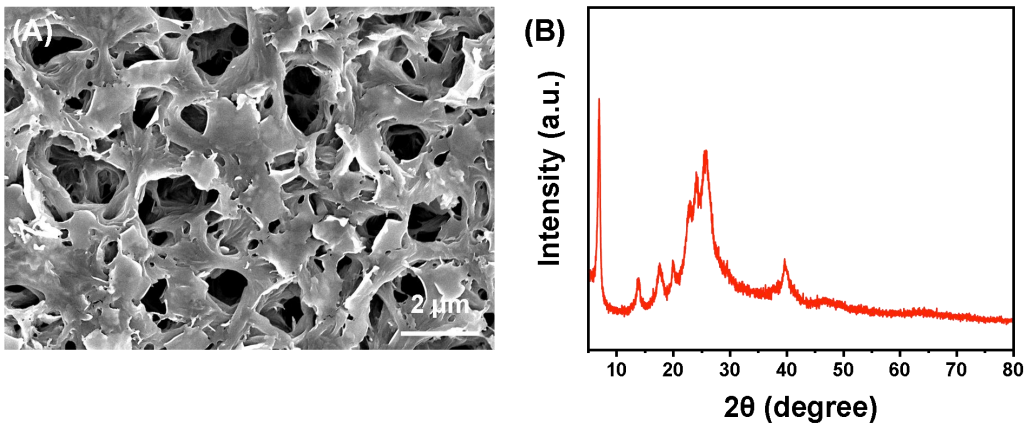

Supplementary Figure 3. (A) SEM image and (B) XRD spectra of the EtDAB·$4PbI_2$ film.

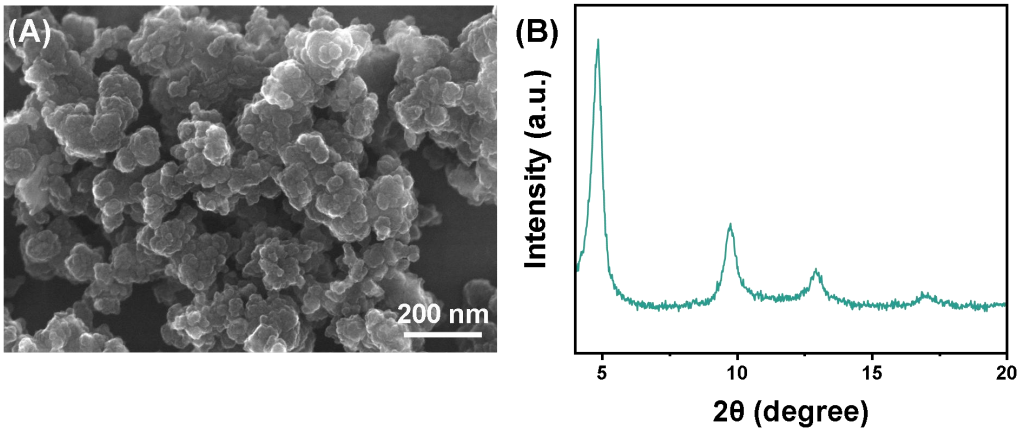

Supplementary Figure 4. (A) SEM image and (B) XRD spectra of $Co_3(HITP)_2$.

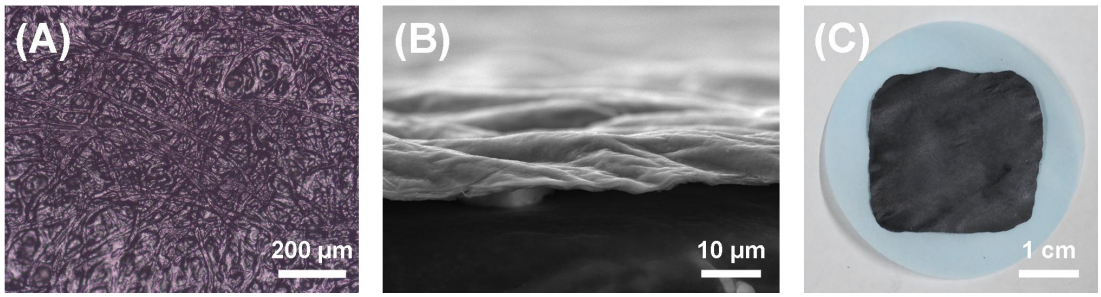

Supplementary Figure 5. (A) Optical micrograph, (B) cross-sectional SEM image and (C) digital image of the MXene film.

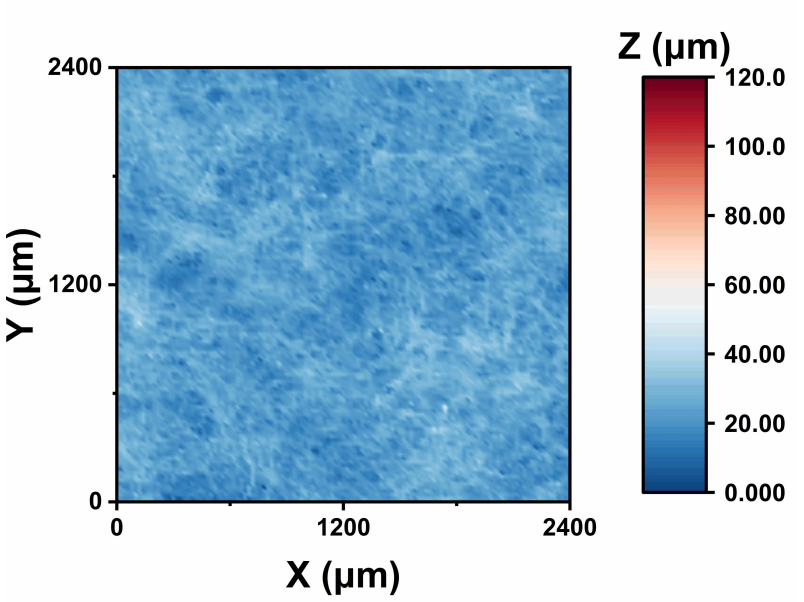

Supplementary Figure 6. The macroscopic surface morphology of the unprinted MXene film.

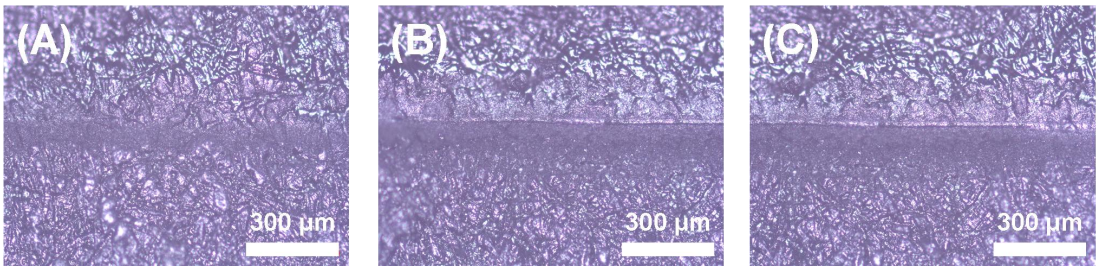

Supplementary Figure 7. Optical micrographs of (A) low, (B) medium, and (C) high stripes.

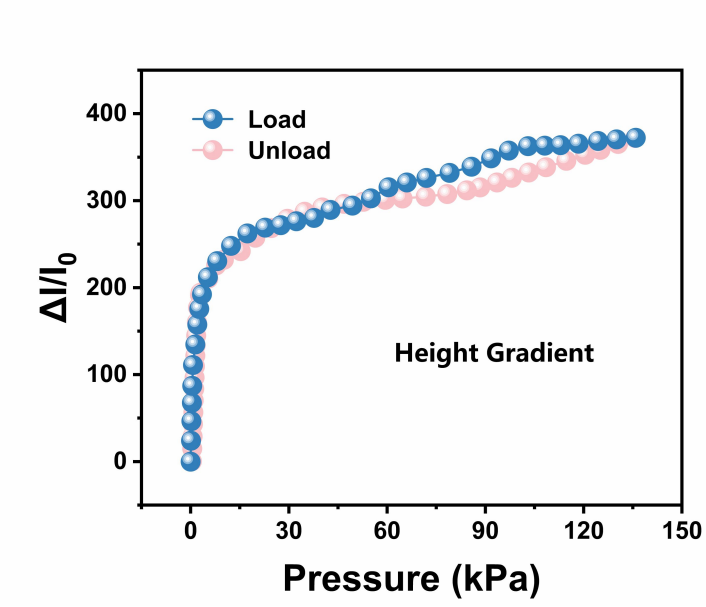

Supplementary Figure 8. Loading–unloading response curves of the pressure module with a single height gradient.

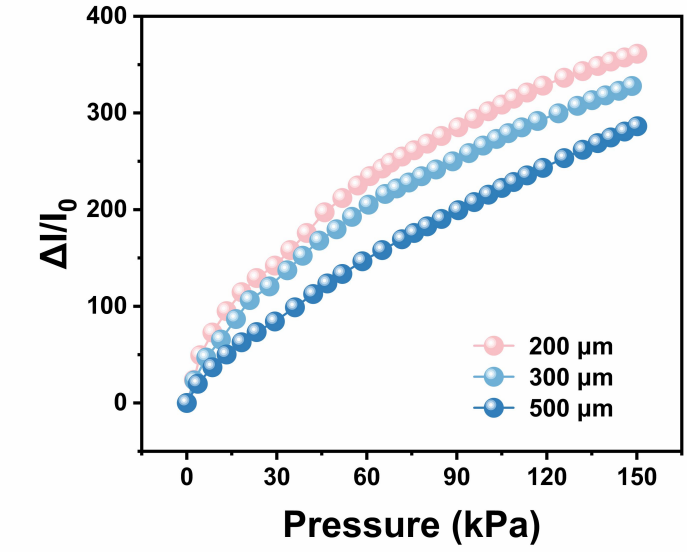

Supplementary Figure 9. Effect of stripe width on pressure sensing behavior.

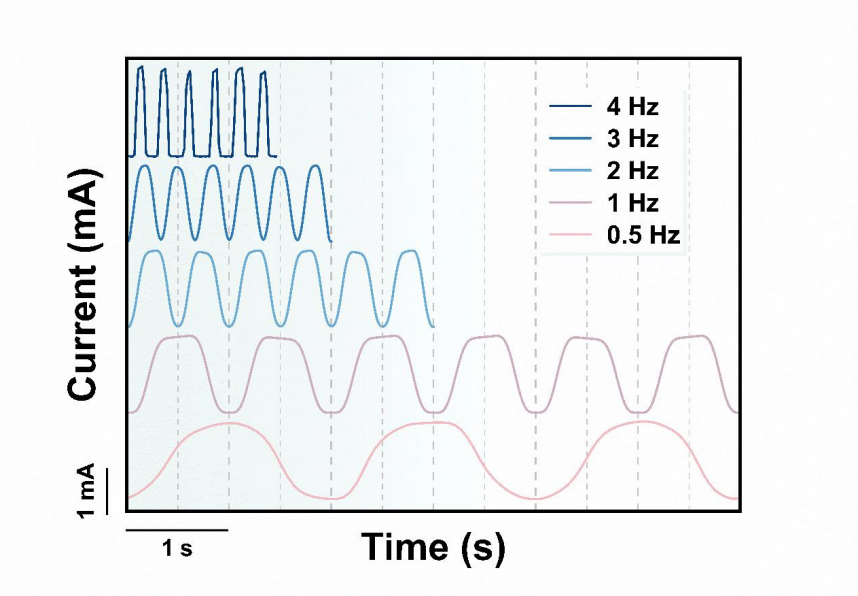

Supplementary Figure 10. Current response of the pressure module under variable frequency.

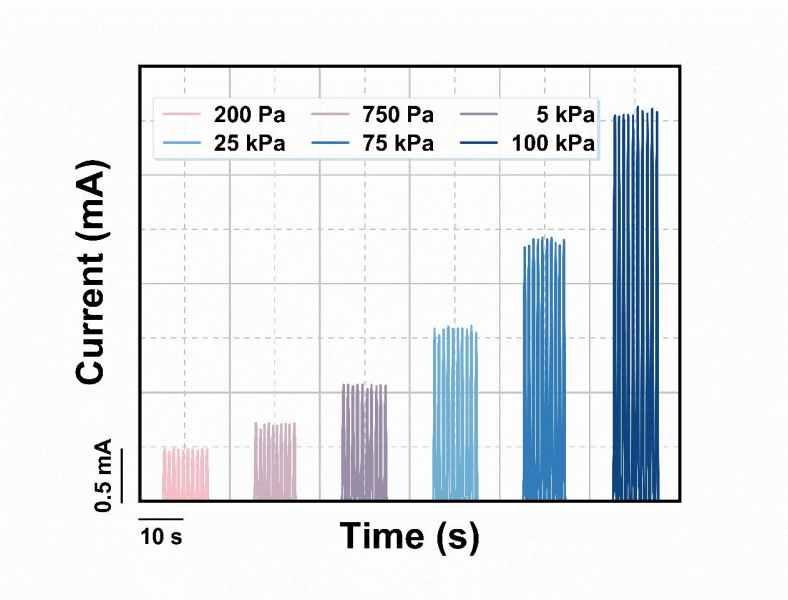

Supplementary Figure 11. Stepwise response of the pressure module under different applied pressures.

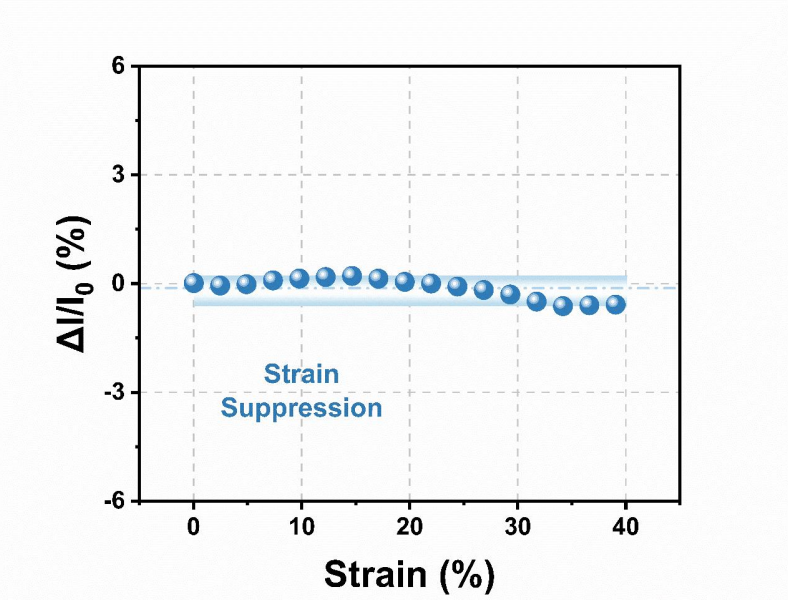

Supplementary Figure 12. Relative current versus strain curve of the pressure module.

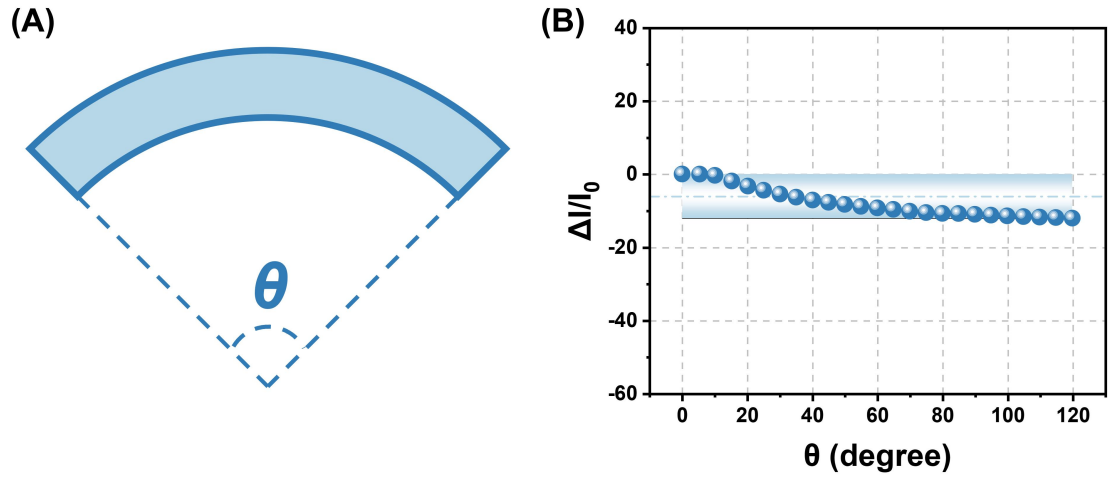

Supplementary Figure 13. Flexibility test of the pressure module. (A) Schematic illustration of the bending angle (θ). (B) Relative current variation of the pressure module under different bending angles.

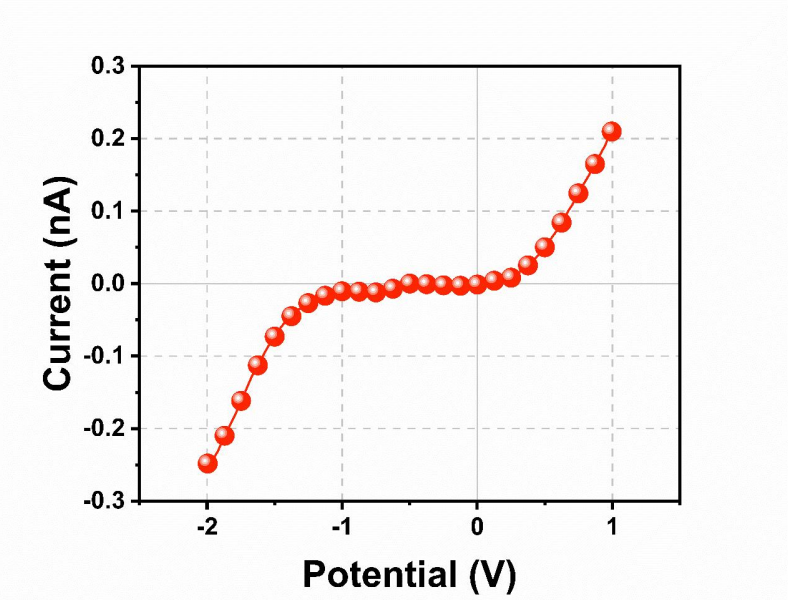

Supplementary Figure 14. Current–voltage (*I*–*V*) characteristics of the temperature module.

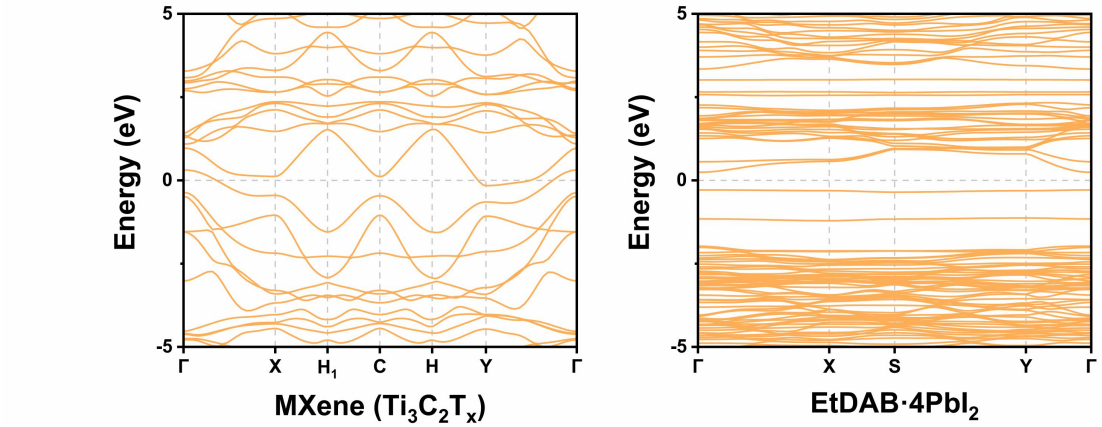

Supplementary Figure 15. Calculated energy band structure of MXene and EtDAB·4PbI$_2$.

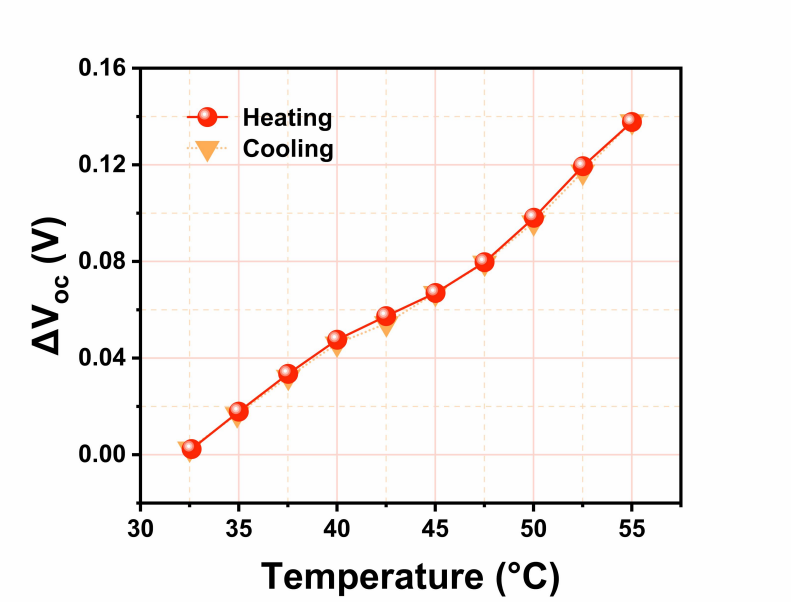

Supplementary Figure 16. Temperature response under repeated heating–cooling cycles.

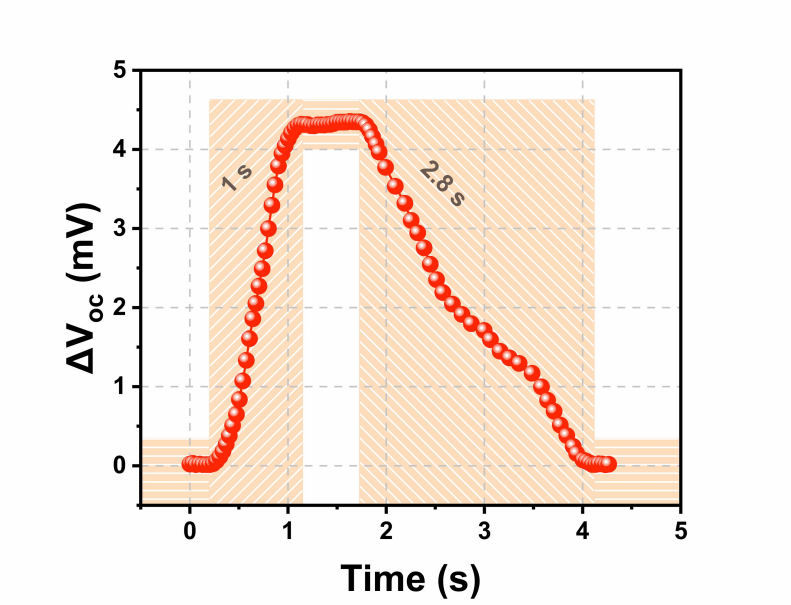

Supplementary Figure 17. Response and recovery time of the temperature module.

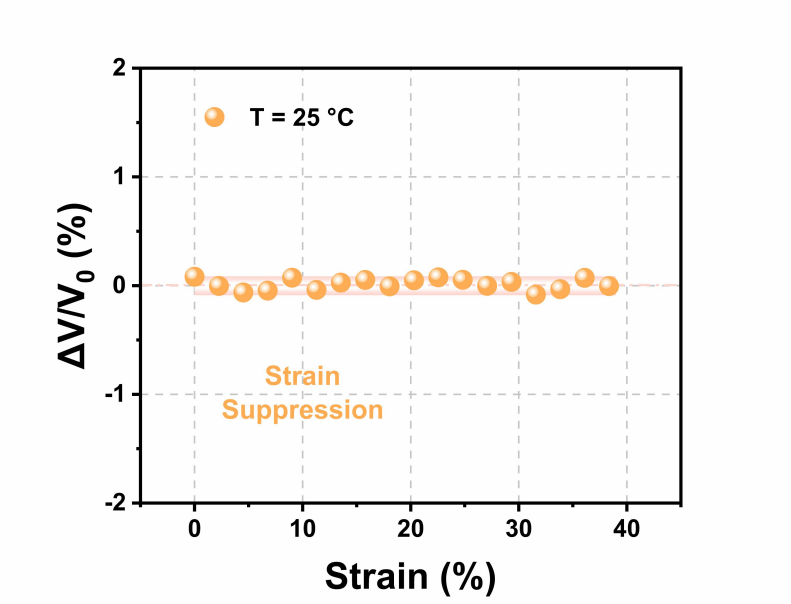

Supplementary Figure 18. Relative V_{oc} variation versus strain curve of the temperature module at 25 °C.

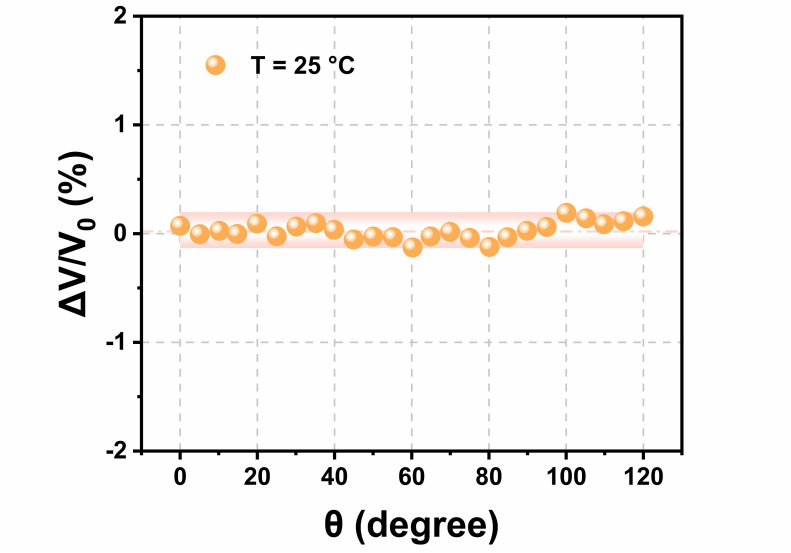

Supplementary Figure 19. Relative V_{oc} variation of the temperature module under different bending angles.

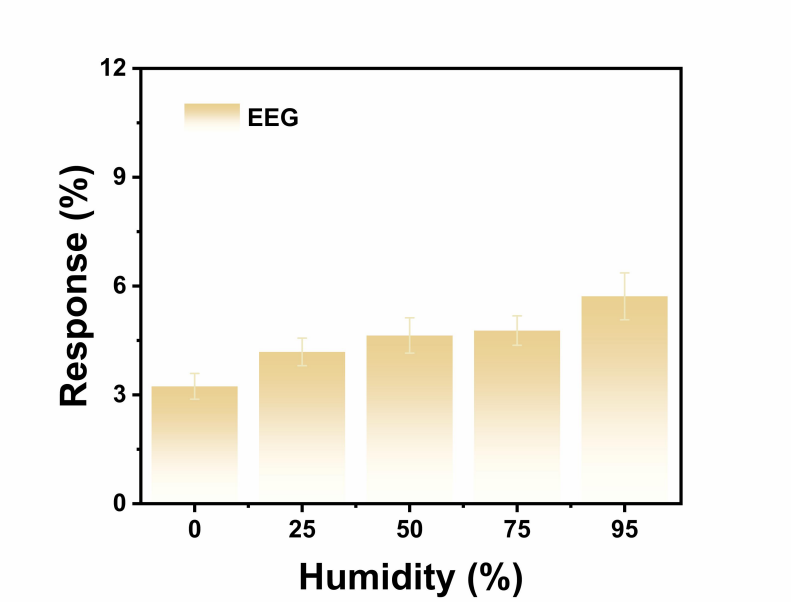

Supplementary Figure 20. NO sensing response of the electrochemically exfoliated graphene (EEG) under different relative humidity conditions. The error bars represent the standard deviation based on a sample size of three (n = 3).

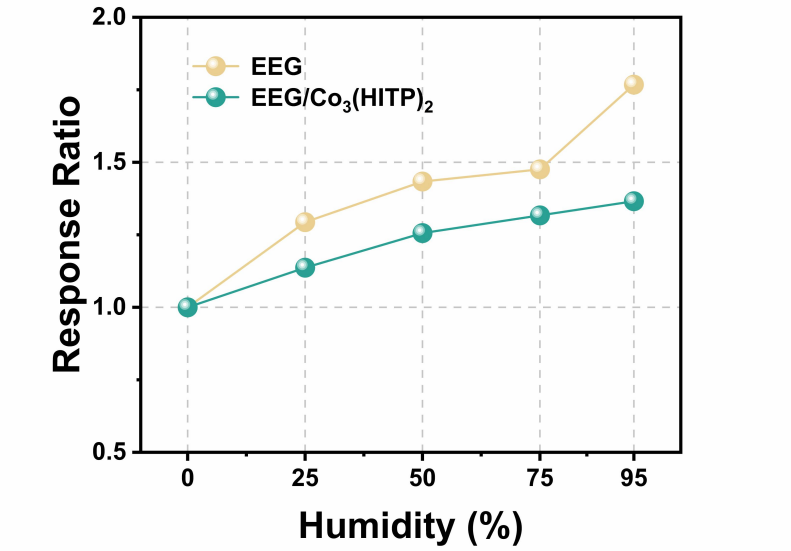

Supplementary Figure 21. Normalized relative variation of the NO sensing response under different relative humidity conditions.

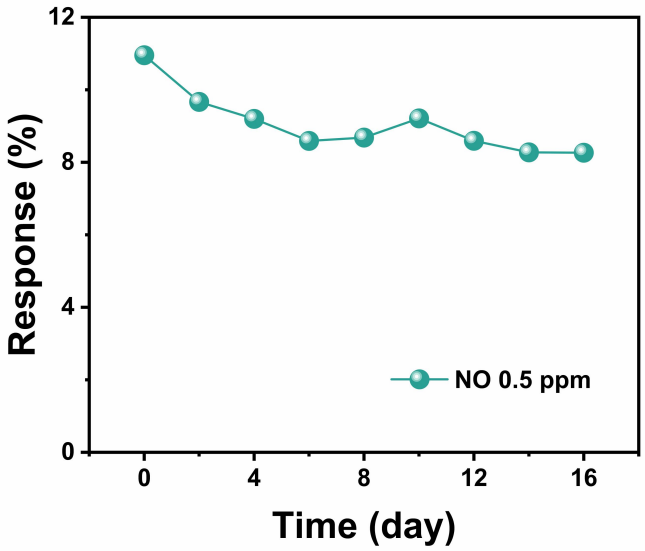

Supplementary Figure 22. Long-term NO response stability of the gas module.

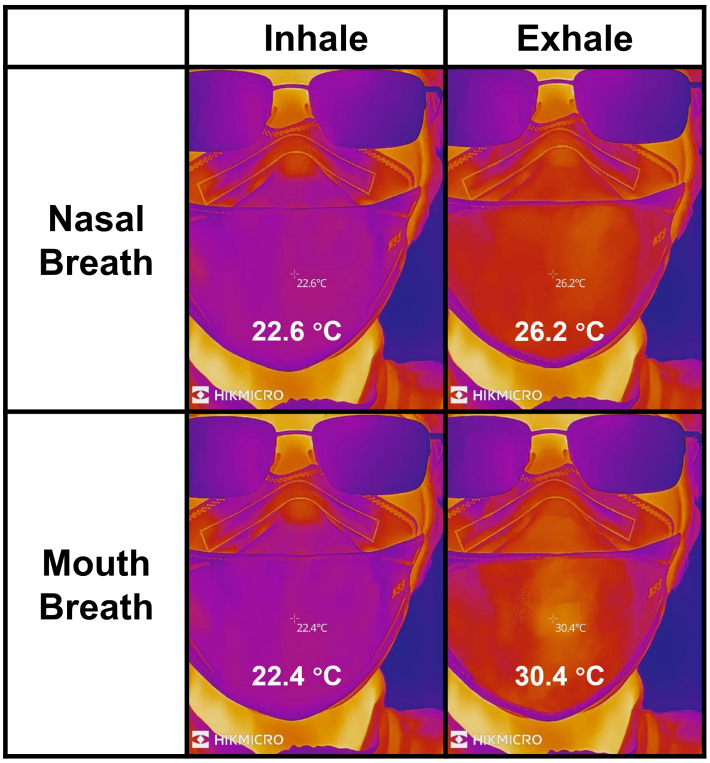

Supplementary Figure 23. Infrared thermal images of the mask during nasal breath and mouth breath.

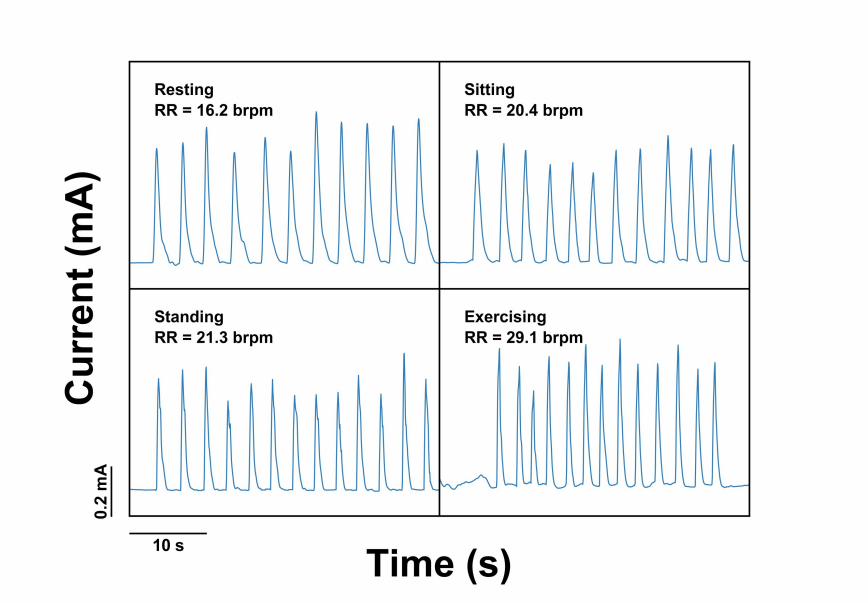

Supplementary Figure 24. Respiratory rate (RR) signals recorded by the mask under different activity states, including resting, sitting, standing, and exercising.

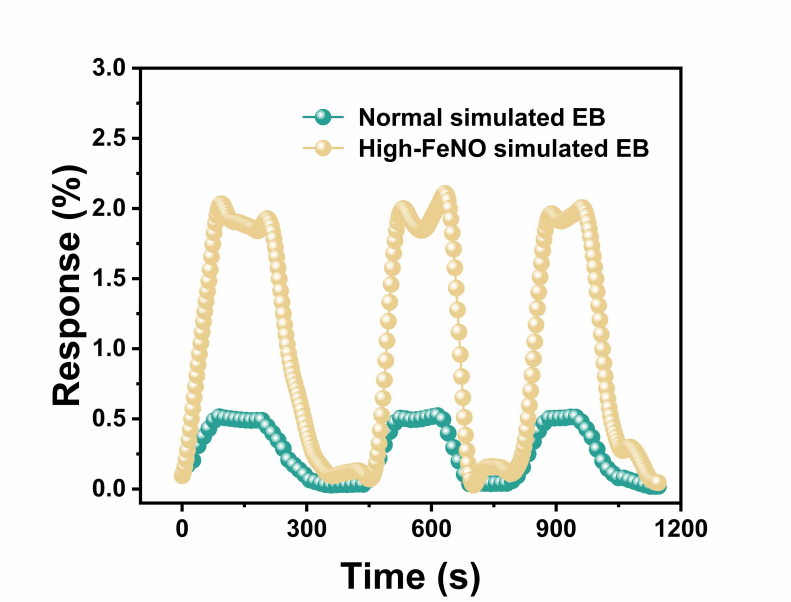

Supplementary Figure 25. Response of the mask to normal simulated EB and high-FeNO simulated EB.

Supplementary Table

Supplementary Table 1. Comparison of key performance metrics of previously reported pressure–temperature sensors

Reference	Materials	Mechanism	Linear range (kPa)	LOD (Pa)	Response time (ms)	Resolution (Temperature) (K)	Decoupling
This work	MXene ($Ti_3C_2T_x$)/EtDAB·$4PbI_2$	Piezoresistive–Junction potential	160	1.9	18	0.1	1
Ref. 37[1]	Graphene coated TPU/CNFs porous sponge	Piezoresistive–Thermoelectric	120	56	25	0.05	1
Ref. 38[2]	3D spacer fabric/PEDOT:PSS	Piezoresistive–Thermoelectric	150	200	80	0.1	1
Ref. 39[3]	MXene ($Ti_3C_2T_x$)/PI flexible composite	Piezoresistive–Thermoelectric	100	< 4000	97	0.4	1
Ref. 40[4]	Wood sponge/PEDOT:PSS/GOPS	Piezoresistive–Thermoelectric	20	40	108	0.1	1
Ref. 41[5]	Graphene/PDMS sponge	Piezoresistive–Thermoelectric	50	100	67	1	0.5

Supplementary Notes

Supplementary Note 1. Calculation of energy band shifts.

The energy band shifts are estimated by the following formula:

$$\Delta E_C = \alpha_L \times \Delta T \times E_C \quad (1)$$

$$\Delta E_V = \alpha_L \times \Delta T \times E_V \quad (2)$$

Here, ΔE_C and ΔE_V represent CBM and VBM shifts, respectively. α_L refers to the linear expansion coefficient. E_C and E_V stand for the deformation potential of the conduction band and valence band, respectively. ΔT means the change in temperature.

Supplementary Note 2. Data normalization for Figure 3H and Supplementary Table 1.

For pressure linear range, min–max normalization was applied:

$$x' = \frac{x - x_{\min}}{x_{\max} - x_{\min}} \tag{3}$$

For response time and temperature resolution, reciprocal transformation was first applied, followed by min–max normalization:

$$x^* = \frac{1}{x} \tag{4}$$

$$x' = \frac{x^* - x^*_{\min}}{x^*_{\max} - x^*_{\min}} \tag{5}$$

For the limit of detection, a logarithmic transformation was employed prior to normalization:

$$x' = \frac{\log_{10} x_{\max} - \log_{10} x}{\log_{10} x_{\max} - \log_{10} x_{\min}} \tag{6}$$

To avoid zero values and improve visualization in the radar plot, all normalized values were further linearly rescaled to the range of 0.1–1:

$$x'' = 0.1 + 0.9x' \tag{7}$$

The decoupling capability was evaluated based on the sensing mechanism and device architecture reported in the literature. Studies achieving intrinsic decoupling at the device level were assigned a value of 1. Studies that mitigate signal interference through non-intrinsic strategies, such as algorithmic processing, structural design, or spatial separation, were assigned a value of 0.5. Studies without dual- or multi-functional sensing capability were assigned a value of 0.

All data were extracted from the corresponding references and processed using the same normalization procedure to ensure consistency and fairness in comparison.

REFERENCES

1. Yin, Y.; Wang, Y.; Li, H.; et al. A flexible dual parameter sensor with hierarchical porous structure for fully decoupled pressure–temperature sensing. *Chem. Eng. J.* **2022**, *430*, 133158, doi:10.1016/j.cej.2021.133158.
2. Li, M.; Chen, J.; Zhong, W.; et al. Large-Area, Wearable, Self-Powered Pressure–Temperature Sensor Based on 3D Thermoelectric Spacer Fabric. *ACS Sens.* **2020**, *5*, 2545–2554, doi:10.1021/acssensors.0c00870.
3. Zhang, X.; Gong, Y.; Xie, F.; Sun, P.; Jiang, S. Dual-Mode Temperature–Pressure MXene Sensor for Enhanced Firefighter Safety and Deep Learning-Enhanced Smart Gloves. *ACS Appl. Mater. Interfaces* **2025**, *17*, 38280–38287, doi:10.1021/acsami.5c09442.
4. Wang, N.; Xia, Z.; Yang, S.; et al. Pressure-temperature dual-parameter sensors designed by wood-derived thermoelectric composites: Micro-pressure high sensitivity. *Compos. Part B Eng.* **2023**, *264*, 110928, doi:10.1016/j.compositesb.2023.110928.
5. Wang, Y.; Wu, H.; Xu, L.; et al. Hierarchically patterned self-powered sensors for multifunctional tactile sensing. *Sci. Adv.* **2020**, *6*, eabb9083, doi:10.1126/sciadv.abb9083.